Science Press

ARTICLE

Preparation and Characterization of CeO$_2$-based Oxygen Storage Materials

Li Hongmei[1,2],   Lan Li[1],   Liu Dayu[1],   Wang Wei[1],   Xue Huiling[1],   Qi Wensheng[1],
Gong Maochu[2],   Chen Yaoqiang[2]

[1] *Chengdu University, Chengdu 610106, China,* [2] *Key Laboratory of Green Chemistry & Technology, Ministry of Education, Sichuan University, Chengdu 610064, China*

Abstract: Four types of CeO$_2$-based oxide storage materials were prepared by co-precipitation, and their physicochemical properties were characterized by X-ray diffraction (XRD), Raman spectroscopy, N$_2$ adsorption-desorption (BET), H$_2$-temperature-programmed reduction (H$_2$-TPR), oxygen pulsing technique, X-ray photoelectron spectroscopy (XPS) and scanning electron microscopy (SEM). XRD patterns reveal that only characteristic peaks of CeO$_2$ are observed in the CeO$_2$ and CeO$_2$-Al$_2$O$_3$ (CA), while CeO$_2$-ZrO$_2$ (CZ) and CeO$_2$-ZrO$_2$-Al$_2$O$_3$ (CZA) show Ce$_{0.75}$Zr$_{0.25}$O$_2$ phases. XPS studies show that 4+ and 3+ oxidation states of cerium coexist on the surface of CZ, CA and CZA. However, almost no 3+ oxidation state is detected in pure CeO$_2$. The best textural properties, higher oxygen storage capacity (OSC) and excellent thermal stability are obtained for CZA. In addition, in order to compare the differences among the four samples, a new insight is proposed that Al^{3+} might be inserted into the inter-space of the fluorite structure or highly dispersed in the solid solution. CZA solid solution may consist of interstitial solid solution and substitutional solid solution, which can be verified by the presence of two oxide species or two types of oxygen channels in CA and CZA. However, the evidence is not detailed enough to support this argument, so further investigation is necessary.

Key words: CeO$_2$-based oxides; thermal stability; Co-precipitation; oxygen storage capacity (OSC); Ce atom utilization ratio

---

Three-way catalysts (TWCs) have been designed to simultaneously remove CO, NO$_x$, and HC, which are the main pollutants from gasoline vehicles[1]. Alumina and oxygen storage materials (OSM) are two key supports for TWCs. Alumina has high surface area and excellent thermal stability, and OSM can keep the air/fuel ratio close to the stoichiometric value, at which all the pollutants can be removed simultaneously[1-4]. However, with increasing the temperature (> 850 °C), OSM is sintered easily, which results in deactivation of the catalysts. Soon after, a novel support CeO$_2$-ZrO$_2$-Al$_2$O$_3$ is designed. For instance, Zhu et al[5] prepared CeO$_2$-ZrO$_2$ and CeO$_2$-ZrO$_2$-Al$_2$O$_3$ and compared their performance. Kašpar and coworkers[6] reported that the modification of Ce-Zr by Al$_2$O$_3$ can improve the thermal stability and enlarge the OSC of the support.

CeO$_2$-ZrO$_2$-Al$_2$O$_3$ (CZA) has been designed and expected to maintain excellent textural properties, thermal stability of alumina and large OSC of the OSM simultaneously. Yao et al[7] implied that highly dispersed zirconia can prevent CeO$_2$ from reacting with Al$_2$O$_3$ in CZA. Ozawa et al[8] reported that the OSC of CZA can be improved by adding ZrO$_2$ and CeO$_2$. Monte et al[9] proposed that adding Al$_2$O$_3$ in the OSM can improve the thermal stability, specific surface area and dynamic-OSC. Morikawa et al[10] discovered that the addition of Al$_2$O$_3$ acts as a "diffusion barrier" at nanometer scale and great improvement of OSC can be achieved. Chen et al[11] observed that the incorporation of Al$_2$O$_3$ can increase the dispersion of Ce$_x$Zr$_{1-x}$O$_2$. Chuang et al[12] indicated that the mixing extent of constituents in

---

Al_2O_3-$Ce_{0.5}Zr_{0.5}O_2$ powders plays a crucial role in the thermal stability, phase composition, textural and OSC property. Wang et al[13] prepared CZA by different methods and testified that the initial strong interaction of CZ and Al_2O_3 can prevent the phase segregation of CZ and phase transformation of Al_2O_3. Huang[14] pointed out that Al^{3+} and Zr^{4+} insert into CeO_2 lattice, resulting in the formation of CeO_2-ZrO_2-Al_2O_3 solid solution.

The purpose of this research is to investigate the physicochemical properties of CZA and the presence form of Al_2O_3 in CZA prepared by co-precipitation method. For comparison, CeO_2, $Ce_{0.75}Zr_{0.25}O_2$ (CZ) and CeO_2-Al_2O_3 (CA) samples were also prepared. The physicochemical properties of the samples were also characterized.

1   Experiment

1.1   Sample preparation

CeO_2, $Ce_{0.75}Zr_{0.25}O_2$ (CZ), CeO_2-Al_2O_3 (CA), and $Ce_{0.75}Zr_{0.25}O_2$-Al_2O_3 (CZA) were prepared by co-precipitation method (the mass fraction of Al_2O_3 in CA and CZA was 50 wt%). First, required amounts of $Ce(NO_3)_3 \cdot 6H_2O$ and $ZrO(CO_3)$ were completely dissolved in water and nitric acid solution, respectively. Then a mixed salt solution was obtained by mixing them together and stirring well. Afterwards, 30 wt% H_2O_2(aq) was added to the above solution. And an excessive amount of ammonia solution was precipitated in the obtained mixed solution. During the process, the pH value was maintained around 10. Thereafter, the obtained precipitates were aged at 100 °C for 5 h, which were then filtered, washed with distilled water, and dried at 90 °C for 24 h to obtain the dry powder samples. Finally, the precipitate powders were calcined at 600 °C for 5 h to obtain the fresh samples. The aged samples were obtained by thermal treating the fresh samples at 1000 °C for 5 h.

The four fresh materials were used as carriers to prepare the Pd catalysts. $Pd(NO_3)_2$ aqueous solution was used as the metal precursor and wet-impregnation method was applied. After $Pd(NO_3)_2$ was impregnated, the obtained powders were dried at 120 °C for 2 h and calcined at 550 °C for 3 h. Thereafter, the samples were introduced into distilled water to obtain slurries, which were coated onto the cylindrical cordierite monolith (Corning, USA, 400 cells/in², 2.5 mL). The nominal Pd content was 0.5 wt% and the washcoat loading was 160 g/L. The monolithic catalysts were dried at 120 °C for 2 h and calcined at 550 °C for 3 h to get the fresh samples (Pd/CeO_2, Pd/CZ, Pd/CA and Pd/CZA), which were further calcined at 1000 °C for 5 h to obtain the aged catalysts, named as Pd/CeO_2a, Pd/CZa, Pd/CAa and Pd/CZAa, respectively.

1.2   Characterization of samples

Powder X-ray diffraction (XRD) were performed on an X'pert Philips diffractometer (Holland), using Cu Kα radiation (λ=0.154 06 nm), 40 kV, 40 mA, $2\theta = 10°\sim90°$ with an interval of 0.03°.

Raman characterization was performed on SPEX Ramalog 1403 (America) laser Raman analyzer using argon at 514.5 nm as an excitation source. The laser power was 150 mW. The scanning range was $200\sim1500$ cm^{-1} and the interval time was 0.15 s. The data were analyzed on SPEX datamate.

Textural properties of samples were measured by N_2 adsorption-desorption on Autosorb-ZXF-05 (Xibei Institute of Chemical Engineering, China). Prior to the measurement, the samples were evacuated at 390 °C for 3 h.

Total OSC was measured after reducing the sample (200 mg) at 550 °C under flowing H_2. OSC was measured at 200 °C by injecting oxygen pulses into the sample until no oxygen consumption can be detected by thermal conductivity detector.

Temperature-programmed reduction (H_2-TPR) experiments were carried out in a conventional system equipped with a thermal conductivity detector. All samples (100 mg) were pretreated in a N_2 flow at 400 °C for 1 h, and then cooled down to room temperature. The reduction was carried out in a flow of H_2 (5 vol%)/N_2 (20 mL·min^{-1}) from 100 °C to 900 °C with a linear heating rate of 10 °C·min^{-1}.

X-ray photoelectron spectroscopy (XPS) experiments were carried out on a spectrometer (XSAM-800, KRATOS Co.) with Al Kα radiation under UHV, and calibration was performed internally using C 1s binding energy (BE) of 284.8 eV. The surface morphology of the samples was observed by scanning electron microscopy (SEM) with JSM-5900LV (Japan) electron microscope operated at 20 kV on specimens.

The three-way catalytic performance of the catalysts was evaluated in a fixed-bed continuous flow reactor. The simulated exhaust gas consisted of C_3H_8 (600 µL/L), CO (0.86%), NO (800 µL/L), CO_2 (12%), H_2O (10%) and balance N_2. The gas hourly space velocity (GHSV) was 40 000 h^{-1}. The conversion of C_3H_8, CO and NO was detected with an FGA-4100 analyzer (Foshan, China). The λ value, which is defined as λ=(2[O_2]+[NO])/(10[C_3H_8]+[CO]), represents the ratio between the available oxygen and oxygen needed for full conversion of C_3H_8, CO and NO. λ=1 was used at each testing point. Prior to the measurement, the catalyst was pretreated under reactive gas mixture at 550 °C for at least 1 h.

2   Results and Discussion

2.1   Structural characterization

The XRD patterns of the fresh samples are displayed in Fig.1. The main peaks of CeO_2 and CA are consistent with the characteristic peaks of cubic fluorite CeO_2, while the

XRD patterns of CZ and CZA show the single fluorite $Ce_{0.75}Zr_{0.25}O_2$ phase. In fact, the fluorite cubic structure of CeO_2-based OSM is perfect, because it has larger oxygen mobility channel than the tetragonal phase[15].

From the XRD patterns of the aged samples (Fig.2), it can be seen that perfectly homogeneous ceria-zirconia solid solution is maintained in CZ sample. Aged CA and CZA also show homogenous cubic fluorite structure. According to research of Monte and Kaŝpar[16] it can be inferred that homogenous solid solutions are formed in CZ, CA and CZA.

Lattice parameters of the samples are listed in Table 1. The lattice parameters measured by XRD are 0.541 44 and 0.536 40 nm for fresh CeO_2 and CZ, and 0.541 32 and 0.536 35 nm for aged CeO_2 and CZ, respectively. The crystal cell shrinkage is originated from the replacement of part of Ce^{4+} (0.097 nm) and Ce^{3+} (0.114 nm) by smaller Zr^{4+} (0.084 nm), indicating that substitutional solid solution is formed for CZ compound. It is worth noting that the lattice parameter of CA is approximately equal to that of CeO_2, while the lattice parameter of CZA is similar to that of CZ. The aged samples show the same phenomenon. So it is proposed that Al may insert into the inter space of the fluorite structure or is highly dispersed in the solid solution. As Xu pointed out[17] that the requirement for the formation of interstitial solid solution is that the radii difference $\Delta r > 41\%$. The ionic radii of Ce^{4+} (0.097 nm) and Al^{3+} (0.054 nm) can fulfill this demand. The possible sketch maps of CZ, CA and CZA are shown in Fig.3. The substitutional solid solution of CZ, interstitial solid solution of CA, mixture of interstitial and substitutional CZA solid solution are proposed.

Crystallite sizes of all samples were estimated applying the Scherrer equation. As shown in Table 1, the average crystallite size of CZA shows the smallest increase upon aging, suggesting the best thermal stability of CZA. It is well known that the aging treatment promotes the growth of
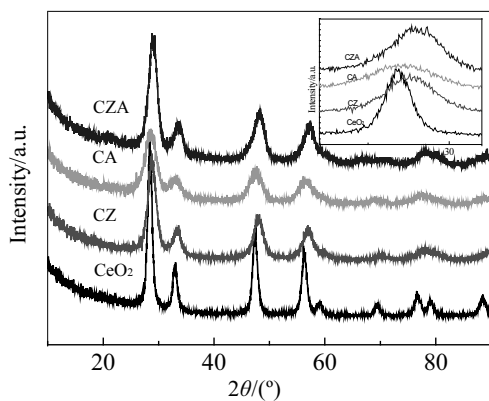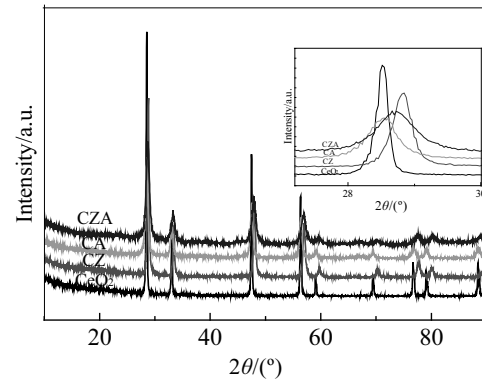

Fig.2   XRD patterns of aged samples

Table 1   Lattice parameter and crystallite size of the samples

Sample	Lattice parameter/nm		Crystallite size/nm	
	600 °C	1000 °C	600 °C	1000 °C
CeO_2	0.54144	0.54132	9.6	50.0
CZ	0.53640	0.53635	6.2	36.2
CA	0.54131	0.54120	4.9	17.3
CZA	0.53723	0.53712	5.5	11.1

CeO_2-ZrO_2 CeO_2-Al_2O_3 CeO_2-ZrO_2-Al_2O_3
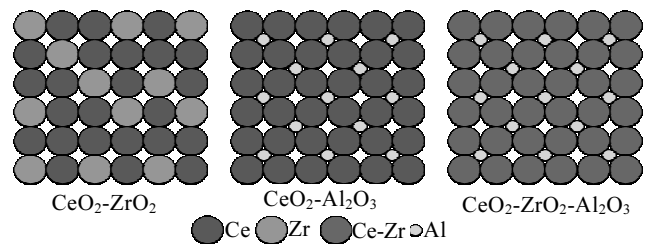
Ce   Zr   Ce-Zr   Al

Fig.3   Schematic representation of the structure of CZ, CA and CZA

crystallites. This work verifies this viewpoint that the addition of Zr and Al has a positive effect on the anti-aging property of CeO_2[18].

The Raman spectrum of aged CZA is shown in Fig.4. The sample shows an intense peak at 468 cm^{-1}, which is attributed to the Raman active mode of F_{2g} symmetry of CeO_2. The weak and broad peak at 570 cm^{-1} is assigned to the weak Raman signal produced by the partial breaking of Raman active oscillation mode of F_{2g} symmetry[19]. The Raman spectrum indicates that aged CZA can keep CeO_2-based cubic fluorite structure, which is consistent with the results of XRD.

2.2   Textural properties

Table 2 summarizes the textural properties of all samples, including specific surface area S_{BET} and pore volume V_s. For comparison, estimated specific surface areas of the samples are listed in Table 3.
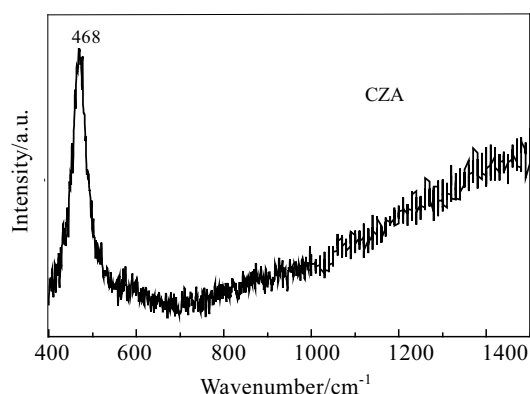

Fig.1   XRD patterns of fresh samples

Fig.4   Raman spectrum of aged CZA

Table 2   Textural properties of the fresh and aged samples

Sample	S_{BET}/m^2·g^{-1}		V_s/mL·g^{-1}		Mean pore size/nm	
	Fresh	Aged	Fresh	Aged	Fresh	Aged
CeO$_2$	99	33	0.17	0.13	5.8	13.8
CZ	107	37	0.21	0.14	5.1	11.7
CA	212	77	0.30	0.27	5.4	10.2
CZA	189	90	0.42	0.29	8.2	9.4

As seen from Table 2, fresh CA shows the largest specific surface area (212 m^2·g^{-1}), which is also larger than the estimated value (163 m^2·g^{-1}). In addition, the specific surface area of CZ is 107 m^2·g^{-1}, which is slightly larger than the estimated one (99 m^2·g^{-1}), indicating that the introduction of Al and Zr, especially Al, can play a positive influence on the specific surface area of CeO$_2$ system. A perusal of the results after aging treatment can give rise to the same conclusion.

Similarly, the specific surface area of fresh CZA is higher than its estimated value as well. Moreover, the specific surface area and pore volume of aged CZA are 90 m^2·g^{-1} and 0.29 mL·g^{-1}, respectively, which are the highest among those of the aged samples, demonstrating the highest thermal stability. When crystallite size is close to the average pore size, it is found from Table 2 that all samples exhibit increased pore sizes upon thermal aging treatment, which is due to the elimination of smaller pores and formation of larger pores associated with the crystallite growth process.

Table 3   Estimated specific surface areas (S_{mixed}) of the samples

Sample	Fresh			Aged		
	CZ	CA	CZA	CZ	CA	CZA
S_{mixed}	99	163	167	33	78	80

Note: estimated specific surface areas of A and B mixtures: S_{mixed} =S_A*A% + S_B*B%

And it is found that the increasing extent of the crystallite size in Table 1 follows the same sequence with that of the average pore size in Table 2. Thus, wider pores and smaller pore volumes are obtained for the aged samples[20]. In addition, it is also worth noting that the average pore size of CZA shows the slightest increase upon aging treatment, which provides further evidence for its highest thermal stability.

2.3   Oxygen storage capability

The OSC results are summarized in Table 4. As can be seen therein, OSC per gram Ce and the utilization ratio of Ce atoms are improved after adding ZrO$_2$ and Al$_2$O$_3$ into CeO$_2$. It can be concluded that the addition of ZrO$_2$ and Al$_2$O$_3$ increases the oxygen mobility. The decrease of OSC after aging may be due to the decreased mobility of oxygen ions induced by the loss of specific surface areas and aggregation of small crystallites. The largest OSC per gram Ce and utilization ratio of Ce atoms are obtained for aged CZA, indicating the highest thermal stability.

In short, Al$_2$O$_3$ and ZrO$_2$ have positive influences on maintaining comparatively larger OSC and ZrO$_2$ shows more remarkable effect. It may be due to the fact that the substitutional solid solution of CZ can better facilitate the enlargement of the lattice space than the solid solution of CA, which is consequently beneficial to the migration of oxygen atoms[11],

2.4   TPR behavior

TPR profiles of all fresh samples are shown in Fig.5. For CeO$_2$, The peak below 700 °C is associated with the reduction of the most easily reduced surface-capping oxygen, while the peak above 800 °C is attributed to the reduction of bulk oxygen[21]. For CZ, there is only one reduction peak,

Table 4   Oxygen storage capability (OSC) of the samples calcined at 600 and 1000 °C

Sample	600 °C				1000 °C			
	CeO$_2$	CZ	CA	CZA	CeO$_2$	CZ	CA	CZA
Ce content/ wt%	81	62	41	31	81	62	41	31
Total OSC	368	550	300	309	118	240	80	172
OSC per gram Ce	452	883	737	992	145	385	197	552
Ce atom utilization ratio/%	25	50	41	56	8	22	11	31

Note: the unit of OSC is μmol O$_2$/g; total OSC is the OSC of practical per gram sample; theoretical OSC per gram Ce (1784 μmol O$_2$/g Ce) was calculated based on the oxygen storage process of 2Ce$_2$O$_3$ + O$_2$ → 4CeO$_2$; practical OSC per gram Ce = total OSC/Ce contents; Ce atom utilization ratio=practical OSC per gram Ce/theoretical OSC per gram Ce

which is due to the increased mobility of bulk oxygen in CZ solid solutions. The TPR profile for CA oxide shows two reduction peaks. One (below 550 °C) is related to the reduction of small crystallites, mainly leading to the formation of CeO_x phase[22], and the other (above 800 °C) is attributed to the formation of $CeAlO_3$ and Ce_2O_3[23,24]. But the XRD patterns show no such species in aged CA sample, which may be due to the great dispersion property of the Al-based material.

The profile of CZA is similar to that of CA, but without the peak of $CeAlO_3$, which means that ZrO_2 is effective in preventing the interaction between ceria and alumina. Compared with CZ, reduction peaks of CA and CZA are split into two regions. It can be inferred that there are two types of oxygen species in CA and CZA, which provide another proof that the way of Al^{3+} incorporation is different from that of Zr. The large difference in oxygen mobility makes it unable to merge the two types of oxygen species into one reduction peak.

In Fig.6, the H_2-temperature programmed reduction (H_2-TPR) profiles of the aged samples are plotted. It is shown that the surface reduction peaks decrease slightly, but the bulk reduction peaks increase to some extent for the CA and CZA samples. It is well known that there is a direct correlation between the peak area and the amount of reductive species. A great decrease of the high-temperature feature is attributed to the decrease of surface reductive species induced by high temperature calcination.
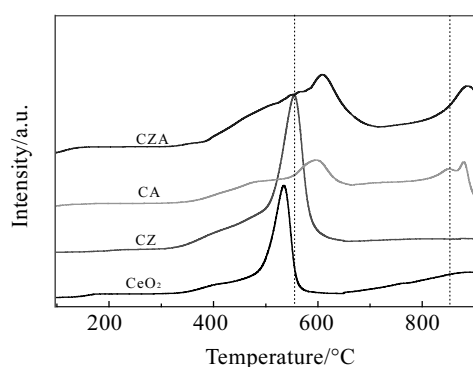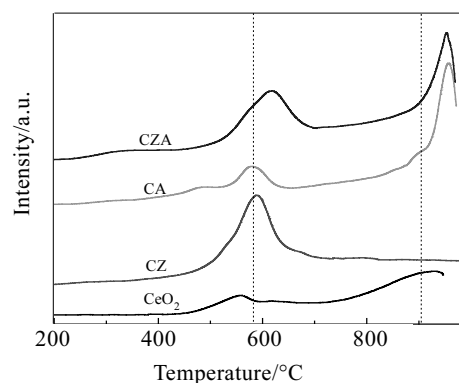

Fig.5　H_2-TPR of fresh samples

Fig.6　H_2-TPR of aged samples

2.5 XPS results

XPS measurements were carried out to investigate the O species and the oxidation state of the cerium element in the samples. Fig.7 shows the Ce 3d XPS spectra of the fresh and aged samples. It can be seen that the Ce 3d peaks are split into $3d_{3/2}$ and $3d_{5/2}$ ionization. The two peaks labeled as V′ and U′ are assigned to Ce^{3+} species, and all others are correlated with Ce^{4+} species[25,26]. The surface percentages of Ce^{3+} are also calculated from the XPS spectra and the data obtained are compiled in Table 5. It can be seen from Table 5 that in CZ, CA and CZA, both Ce^{3+} and Ce^{4+} are present. The concentrations of Ce^{3+} in fresh CZ, CA and CZA are 25.4 at%, 27.1 at% and 35.5 at%, respectively. However, almost no Ce^{3+} is observed in CeO_2. That is to say, the addition of ZrO_2 and Al_2O_3 into CeO_2 promotes the generation of Ce^{3+} species.

After calcination, the concentration of Ce^{3+} in CZ conversely increases, indicating that the addition of ZrO_2 can increase and meanwhile stabilize the concentration of Ce^{3+} in CeO_2. This phenomenon can explain why the performance of TPR and OSC of CZ is more stable at high temperatures than that of pure CeO_2 and CA. The maintenance of Ce^{3+} and Ce^{4+} in the meantime can ensure that the content of oxygen cavity and the ratio of oxygen movement are enough to perform the reversible reaction: $Ce_2O_3 + 0.5O_2 \rightarrow 2CeO_2$[26,27].

The higher the concentration of Ce^{3+}, the larger the number of oxygen vacancies and mobile oxygen atoms. CZA has the maximum concentration of Ce^{3+} among all samples. So CZA possesses the best redox performance. The maximum concentration of Ce^{3+} in CZA is consistent with its highest Ce atom utilization ratio.

Fig.8 shows the O 1s XPS spectra of the fresh and aged samples. Two types of oxygen species can be recognized from the O 1s XPS curves. The peaks located at 530.0~531.0 eV are assigned to the lattice oxygen (hereafter denoted as O_I); other peaks located at 531.0~532.5 eV (hereafter denoted as O_{II}) may be attributed to the adsorbed oxygen (possibly from adsorbed water and/or carbonates or the defect oxygen) [27-29].

The relative content of total O species on the surface and the ratios of O_I/O_{II} are shown in Table 6. Compared with pure CeO_2, the increase of lattice oxygen of CZ (O_I) and surface oxygen of CA (O_{II}) may be ascribed to the following two reasons. (1) Zr can increase the concentration of lattice

Table 5　Surface composition of $Ce^{3+}/(Ce^{3+}+ Ce^{4+})$ of the samples

Sample	600 °C				1000 °C			
	CeO_2	CZ	CA	CZA	CeO_2	CZ	CA	CZA
Content/ at%	-	25.4	27.1	35.5	-	31.4	23.3	34.1

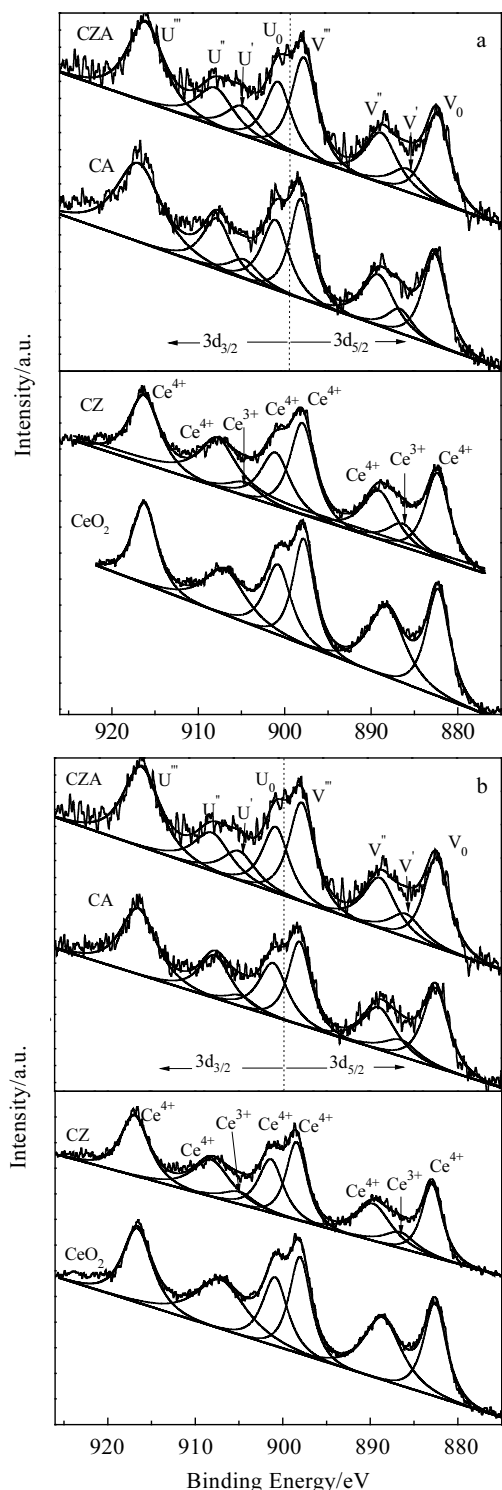Fig.7   Ce 3d XPS spectra of fresh (a) and aged (b) samples

oxygen and Al can increase the concentration of adsorbed oxygen[24-27]. The structural cell shrinkage as a result of the formation of substitutional CZ solid solution leads to higher concentration of lattice oxygen. The increase in specific sur-
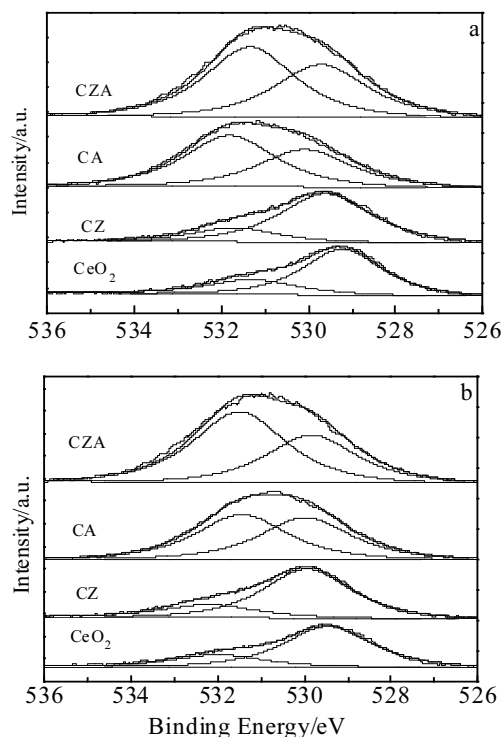

Fig.8   O 1s XPS spectra of fresh (a) and aged (b) samples

face area of CA results in higher concentration of adsorbed oxygen on the surface. The peak areas of surface and lattice oxygen of the CZA solid solution increase. (2) The binding energy of ZrO_2 overlapped with O_I is 530.6 eV and the binding energy of Al_2O_3 overlapped with O_{II} is 531.5 eV[28,30].

2.6   SEM of CZA sample

Fig.9 and Fig.10 show the typical micrographs of the fresh and aged CZA, which clearly show the formation of micro-roundness structure. The average particle diameter increases from 5 μm to 10 μm upon aging treatment, implying only slight sintering of CZA. The particle size observed from the SEM images is larger than the crystallite size measured by XRD. This is because the crystallites measured by XRD are the primary particles of the materials, while

Table 6   Binding energy (BE) and surface atomic composition of O 1s

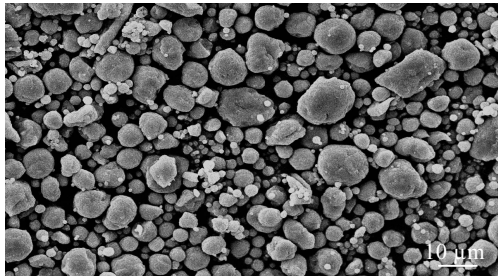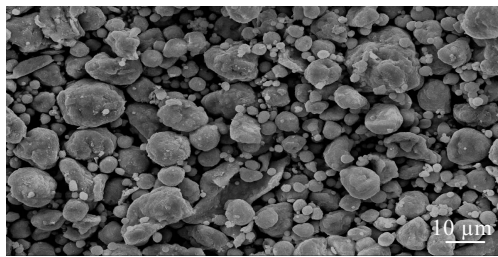| Samples	O 1s (600 °C)			O 1s (1000 °C)		
	BE/eV	O 1s content/ at%	O_I/O_{II}	BE/eV	O 1s content / at%	O_I/O_{II}
CeO_2	529.2 (531.3)	65.9	73.2/26.8	529.5 (531.9)	69.7	76.6/23.4
CZ	529.6 (531.7)	66.9	79.1/20.9	529.9 (532.2)	66.9	77.9/22.1
CA	530.9 (531.8)	68.5	42.6/57.4	530.0 (531.4)	65.2.	48.3/51.7
CZA	529.7 (531.4)	67.5	43.6/56.4	529.8 (531.5)	66.5	39.6/60.4

Fig.9   SEM image of fresh CZA sample

Fig.10   SEM image of aged CZA sample

the particles observed in SEM images are secondary particles, which are composed of a large number of primary particles. Nevertheless, it should be pointed out that the crystallite growth extent observed by XRD technique is close to the particle growth extent detected by SEM, indicating the excellent thermal stability of CZA. Fortunately, the particle diameter of 5~10 μm can meet the requirements of the supports for automobile catalysts at high temperature and high space velocity[31].

2.7   Three-way catalytic performance

The three-way catalytic performance of the supported Pd-based catalysts was evaluated, and the results are presented in Fig.11. For the fresh catalysts, it is found that the catalytic activity follows a sequence of Pd/CZ > Pd/CZA > Pd/CeO$_2$ ≥ Pd/CA. Thus, it seems that the textural property of the support materials exerts almost no influence on the catalytic activity. This is probably due to the high surface area and large pore volume of the samples, which are enough to provide sufficient reaction pathway. Therefore, the differences in the three-way catalytic performance are mainly
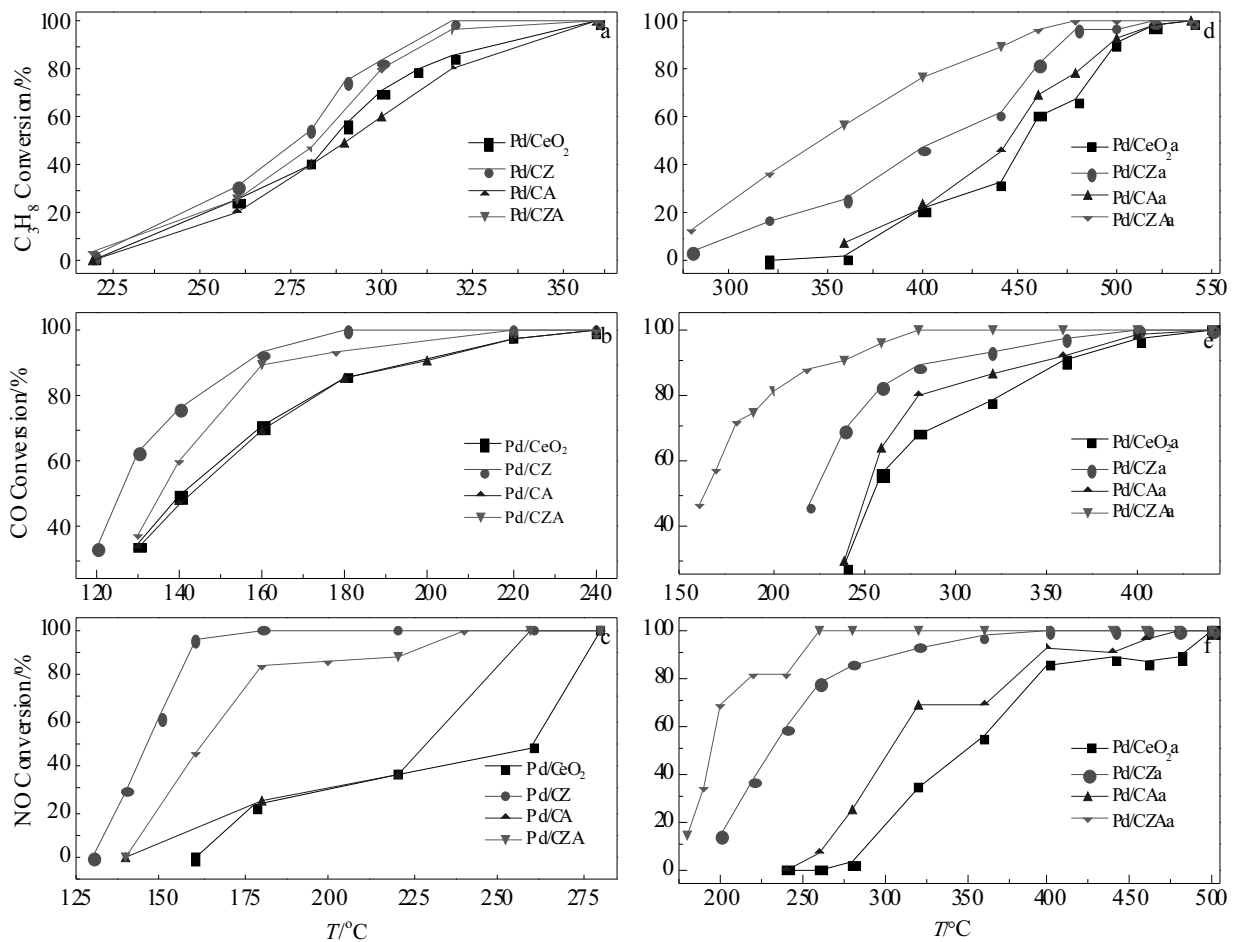

Fig.11   Conversion curves of C$_3$H$_8$, CO and NO as a function of temperature at stoichiometry (λ=1) of the supported fresh (a~c) and aged (d~f) catalysts

dependent on the different redox properties of the samples. As can be found from the OSC and TPR results, the OSC and reducibility of the support materials decrease in the sequence of Pd/CZ > Pd/CeO$_2$ ≥ Pd/CZA > Pd/CA, which is similar to the decreasing sequence of the catalytic performance.

After aging treatment at 1000 °C, the catalysts undergo different extents of deactivation. As shown in Fig.11d, 11e, and 11f, the catalytic reaction takes place at relatively high temperatures, and a decreasing sequence of Pd/CZA > Pd/CZ > Pd/CA > Pd/CeO$_2$ is observed. That is, Pd/CZA possesses the highest thermal stability. A combination of the three-way catalytic performance with the above physicochemical characterization results reveals that the variation tendency of the structural, textural and redox properties can well account for the differences in the three-way catalytic performance of the four aged catalysts. That is, the superior three-way catalytic performance of Pd/CZAa is ascribed to its highest specific surface area, largest pore volume, smallest crystallite size, as well as the excellent redox property.

3   Conclusions

1) Excellent thermal stability, higher oxygen storage capacity (OSC), larger specific surface area, and homogenous solid solution can be obtained for CZA.

2) XRD and Raman results indicate the formation of substitutional solid solution of CZ, interstitial solid solution of CA, mixture of interstitial and substitutional solid solution of CZA and further investigation is necessary.

3) Both 4+ and 3+ oxidation states of cerium in CZ, CA and CZA coexist even after high temperature treatment. There are two different types of oxygen species according to XPS and TPR.

4) CZA possesses a well-dispersed and suitable amorphous particle size. No significant increase in size is observed with increasing the calcination temperature.

5) Among the four supported catalysts, Pd/CZA shows the highest thermal stability in the three-way catalytic performance. That is, after aging treatment, Pd/CZA displays the best three-way catalytic performance, showing potential application in the purification of gasoline engine exhaust.

References

1   Leung E, Lin Q, Farrauto R *et al*. *Catal Today*[J], 2016, 277: 227

2   Chen A, Zhou Y, Ta N *et al*. *Catal Sci Technol*[J], 2015, 5: 4184

3   Zhou Y, Deng J, Lan L *et al*. *J Mater Sci*[J], 2017, 52: 5894

4   Cui Y, Lan L, Shi Z *et al*. *RSC Adv*[J], 2016, 6: 66 524

5   Zhu L, Yu G, Qin W *et al*. *J Alloy Comp*[J], 2010, 492: 456

6   Kašpar J, Fornasiero P, Hickey N. *Catal Today*[J], 2003, 77: 419

7   Yao M, Baird R, Kunz F. *J Catal*[J], 1997, 166: 67

8   Ozawa M, Matuda K, Suzuki S. *J Alloy Compd*[J], 2000, 303-304: 56

9   Monte Di R, Fornasiero P, Kašpar J. *Chem Commun*[J], 2000, 21: 2167

10 Morikawa A, Suzuki T, Kanazawa T. *Appl Catal B: Environ*[J], 2008, 78: 210

11 Lan L, Chen S, Zhao M *et al*. *J Mol Catal A: Chem*[J], 2014, 394: 10

12 Chuang C, Hsiang H, Hwang J. *J Alloy Compd*[J], 2009, 470: 387

13 Wang J, Wen J, Shen M. *J Phys Chem C*[J], 2008, 112: 5113

14 Huang P, Jiang H, Zhang M. *J Rare Earth*[J], 2012, 30: 524

15 Ranga R, Foransiero P, Di Monte R. *J Catal*[J], 1996, 162: 1

16 Monte Di R, Kašpar J. *Mater Chem*[J], 2005, 15: 633

17 Xu Y. *Foundations of Materials Science*[M]. Beijing: Beijing University of Technology Press, 2002: 25

18 Cui Y, Fang R, Shang H *et al*. *J Alloy Compd*[J], 2015, 628: 213

19 Cui Y, Lan L, Shi Z *et al*. *RSC Adv*[J], 2016, 6: 66 524

20 Dumeignil F, Sato K, Imamura M. *Appl Catal A: Gen*[J], 2003, 241: 319

21 Guo J, Shi Z, Wu D *et al*. *J Alloy Compal*[J], 2015, 621: 104

22 Peng N, Zhou J, Chen S *et al*. *J Rare Earth*[J], 2012, 30: 342

23 Yamaguchi T, Ikeda N, Hattori H *et al*. *J Catal*[J], 1981, 67: 324

24 Vasylechkoa L, Senyshyna A, Trots D *et al*. *J Solid State Chem*[J], 2007, 180: 1270

25 He H, Dai H, Wong K *et al*. *Appl Catal A: Gen*[J], 2003, 251: 61

26 Zhong L, Hu J, Cao A *et al*. *Chem Mater*[J], 2007, 46: 2446

27 Vidal H, Kasˇpar J, Pijolat M *et al*. *Appl Catal B: Environ*[J], 2000, 27: 49

28 Wang S, Zheng X, Wang X *et al*. *Catal Lett*[J], 2005, 105: 163

29 Sellick D, Aranda A, García T *et al*. *Appl Catal B: Environ*[J], 2013, 132-133: 98

30 Natile M, Boccaletti G, Glisenti A. *Chem Mater*[J], 2005, 17: 6272

31 Suzuki T, Morikawa A, Sobukawa H. Japanese Patent, EP1020216 B1[P], 2004

CeO$_2$ 基储氧材料的制备和表征

李红梅[1,2]，兰 丽[1]，刘达玉[1]，王 卫[1]，薛慧玲[1]，漆文胜[1]，龚茂初[2]，陈耀强[2]

(1. 成都大学，四川 成都 610106)

(2. 四川大学 绿色化学与技术教育部重点实验室，四川 成都 610064)

摘 要: 用共沉淀法制备了4种CeO$_2$基储氧材料，并用X射线衍射(XRD)，Raman光谱，N$_2$吸附-脱附(BET方法)，H$_2$程序升温还原(H$_2$-TPR)，氧脉冲技术，X射线光电子能谱(XPS)和扫描电子显微镜(SEM)表征了其物理化学性质。XRD结果表明，在CeO$_2$和CeO$_2$-Al$_2$O$_3$ (CA)中只能检测到宽的CeO$_2$的特征峰，而CeO$_2$-ZrO$_2$ (CZ)和CeO$_2$-ZrO$_2$-Al$_2$O$_3$ (CZA)中检测到了Ce$_{0.75}$Zr$_{0.25}$O$_2$相，所有的CeO$_2$基储氧材料中都形成了均匀的固溶体。XPS结果表明，三价铈和四价铈共存于CZ，CA和CZA的表面，而在纯CeO$_2$中几乎检测不到三价铈的存在。CZA表现出了最佳的织构性能，高的储氧量(OSC)和优异的热稳定性。另外，为了阐释4个样品的差异，提出了一种新的观点：Al^{3+}可能插入了萤石结构的间隙或者高度分散在固溶体中。CZA固溶体可能是由间隙型固溶体和置换型固溶体混合组成的，这一点由CA和CZA中存在2种不同的氧化物或者2种类型的氧通道可以证明。然而，关于这个观点的详细证据还不够充分，需要继续进行深入的研究。

关键词: CeO$_2$基储氧材料；热稳定性；共沉淀；储氧量(OSC)；Ce 原子利用率

作者简介：李红梅，女，1980 年生，博士，副教授，成都大学药学与生物工程学院，四川 成都 610106，电话：028-84603251，E-mail: lihongmeihappy@126.com